

Keywords

hyperspectral imaging,
X-ray diffraction,
electron microprobe,
scaling,
Indonesia.

Received: January 20, 2022

Accepted: March 11, 2022

Published: April 02, 2022

Performance of analytical techniques (XRD, EPMA, SWIR imaging) for the identification of minerals frequently formed during natural and technological geothermal processes

Fiorenza Deon ¹, Hans-Jürgen Förster ², Frank van Ruitenbeek ¹, Oona Appelt ²

¹ Faculty of Geo-Information Science and Earth Observation (ITC), University of Twente, 7500 AE Enschede, the Netherlands

² Helmholtz Centre Potsdam GFZ German Research Centre for Geosciences, 14473 Potsdam, Germany

Email address

f.deon@utwente.nl (F. Deon)
Corresponding author

Abstract

This study compares the performance of three analytical methods: X-ray powder diffraction (XRD), electron-microprobe analysis (EMPA), and hyperspectral imaging in the short-wave infrared range (SWIR) for the identification of minerals commonly formed during natural and technological geothermal processes. The samples from three geothermal sites in Indonesia contain a spectrum of minerals, which are characteristic for natural geothermal activities (alunite, jarosite, cristobalite, tridymite) and/or are involved in scaling-forming processes in geothermal plants (barite, celestine, common opal, calcite). We show and discuss the strengths and weaknesses of the individual techniques with respect to properly identify these minerals and to approximate their relative proportions. The SWIR camera permits an unambiguous identification of only a small selection of the geothermally relevant minerals, which restricts its employment as routine tool in the context of applied geothermics. XRD and EMPA are more powerful techniques and deliver complementary information. In case that (a) SWIR inactive species occur, (b) the entire spectrum of minerals present in a sample has to be unequivocally identified, (c) amorphous substances are present, (d) accurate mineral compositions are required, and (e) detailed information on minerals occurring in low abundance and grain size is warranted, the combined use of XRD and EMPA is mandatory.

1. Introduction

The increasing demand of renewable (geothermal) energy resources requires the scientific and industrial community to develop fast and reliable screenings to speed up the recognition of mineral formation processes associated with the operation of geothermal power plants. Especially during the first exploration stage, the decision on which mineral-detection methods will be applied plays a crucial role to reduce the costs of the field campaigns, drilling operations and the general planning of the geothermal/mineral development of a prospect.

The correct identification of potentially harmful secondary minerals aids in a better prediction of potential scaling-forming processes that give rise to clogging of pipes in the plants. Undesired scaling has a serious impact on the operational performance of an active geothermal plant (e.g. Mundhenk et al., 2013; Klapper et al., 2016). The nature of the scaling-forming minerals is primarily related to the temperature and composition of the geothermal fluid and the geology of the area, especially the type of reservoir rocks. Alt-Epping et al., (2013) and Stober (2014) ascribe the precipitation of calcite preferentially to low-moderate enthalpy geothermal systems characterized by carbonate/dolomitic aquifers, with serious consequences on

the plant performance if acting as scaling mineral (Boch et al., 2017). In high enthalpy systems, typically related to active magmatic settings, a typical scaling-forming species is hydrous silica, i.e., common opal (e.g. Gunnarsson and Arnórsson 2005; Zarrouk et al., 2014). Other geothermally relevant minerals are sulfates, such as barite–celestine (Regenspurg et al., 2015), which have the potential to substitute toxic heavy metals and radioactive elements, such as Pb and Ra. Radioactive scaling causes severe challenges for the waste disposal and storage (Schreiber et al., 2013). A correct assessment of the secondary mineralization is, therefore, a powerful tool to guarantee the operational functioning of a plant and prevent clogging–corrosion phenomena, thus avoiding additional costs associated with cleaning operations and the interruption of the production. The correct identification of pore- and fracture-clogging minerals is certainly also in the focus of other recently important strategic missions in the geological subsurface, such as the storage of CO₂ (e.g.: Wu and Li, 2020).

In this paper we compare and discuss the applicability and reliability of three mineral-analytical methods: hyperspectral imaging in the short-wave infrared range (SWIR) (cf. Koike and Kouda, 2016); X-ray powder diffraction (XRD) and electron microprobe analysis (EMPA). The study encompasses three, but representative samples from three geothermal sites in Indonesia: Mount Salak on West Java and the Bajawa area on Flores Island. Many years of geothermal exploration has made Indonesia a suitable place to apply and compare different mineral-analytical techniques. Several geothermal areas, such as Kamojang (Java), have geothermal plants active for many decades (Deon et al., 2015). The hydrothermal mineralogy has been described for several prospects in Indonesia, such as Lahendong (Utami, 2011), Tompaso (Savitri 2016), and Wayang Windu (Bogie et al., 2008).

The samples contain a representative selection of hydrothermal species (jarosite–alunite, celestine–barite, common opal, calcite) that play a crucial role as scaling minerals in geothermal plants and, thus, are particularly attractive for studying their response to widely used analytical techniques (cf. section 3).

We are conscious of the fact that the number of surveyed samples is insufficient as that our study could be rated comprehensive. Whether a certain mineral could be identified with one of the deployed analytical techniques or not is, however, largely independent of the number of studied rocks and their provenance. The study of other factors influencing the sensitivity of an analytical technique, such as the absolute abundance of a particular mineral and the kind and number of associate species, certainly requires a more extensive sample set.

2. Background information

2.1 Methodology

The studied Indonesian samples bear a variety of hydrothermal minerals observed in spatial association with geothermal prospects and hot springs. The question arises whether these species are exceptional or commonplace in these environments and whether their presence has an impact on the productivity and environmental performance of geothermal

plants. Below we will briefly describe what is recently known about the geothermal relations of the minerals detected in the course of this study.

Jarosite and alunite: The hydroxylated potassium iron sulphate jarosite ideally $\text{KFe}_3^{3+}(\text{OH})(\text{SO}_4)_2$, is the most common member of the alunite super-group and the Fe^{3+} -analogue of alunite. Its formation requires very low pH (McCubbin et al., 2009), likely < 3. Jarosite, often associated with alunite, is a typical mineral in epithermal gold deposits, i.e., the gold deposit El-Indio-Pascua Belt, Argentina (Holley et al., 2016).

Jarosite is reported from several geothermal systems, such as Kamojang, West Java, where it is associated with alunite and kaolinite (Utami and Browne, 1999; Utami, 2000). In the Waiotapu geothermal area in New Zealand, jarosite in association with hydrous ferric oxide and lepidocrocite was detected in acidic hot springs (Jones and Jenaut, 2007). In the Orakei Korako geothermal field in New Zealand, crust-forming jarosite precipitated from acidic sulfate pool waters (Rodgers et al., 2000). Other occurrences include the Licancura geothermal field in the Andean Cordillera in Northern Chile and the Los Humeros geothermal system in Mexico.

Jarosite occurring as a scaling product in geothermal wells, pipes and casings has not yet been reported, but it may potentially precipitate. If oxygen-rich geothermal waters interact with reservoir rocks containing pyrite FeS_2 , this and other sulphide minerals will oxidize and build metal-rich solutions of sulphuric acid, or secondary acidic metal sulphate minerals such as jarosite (Banks et al., 2019). Depending on the elemental load of the fluid, jarosite may act as metal trap, for instance for arsenic (Johnston et al., 2012), and, thus, is potentially environmentally hazardous.

Alunite, $\text{KAl}_3(\text{OH})_6(\text{SO}_4)_2$, originates at similar conditions as jarosite, i.e., in acid-vapor dominated hydrothermal systems (cf. Steiner, 1977; Henley and Ellis, 1983). As jarosite, alunite is frequently associated with epithermal gold mineralization, for instance, at Rodalquilar, Spain (Arribas et al., 1996), and at the Tambo high-sulfidation Au deposit, located within the El Indio-Pascua belt in Chile (Deyell et al., 2005).

Alunite accompanying cristobalite (reflecting the assemblage in our sample GOU) was reported by Brehme et al., (2016) as alteration mineral of a basalt in the vicinity of an acidic hot spring in Lahendong, Sulawesi, Indonesia. Additional occurrences in Indonesia comprise the area of the Papandayan volcano, Java, and Sumba. Taguchi et al., (2006) described alunite with cristobalite from the production area of the Otake geothermal field in Japan. Sener et al., (2017) reported alunite, together with jarosite, from the Cappadocia geothermal province in Turkey. Other occurrences in geothermal fields include Hatchobaru, Kyushu, Japan, and Copahue, Argentina, only to mention a few. Alunite, as jarosite, can be used to determine the age of fossil alteration and geothermal processes by ^{40}Ar – ^{39}Ar dating (Holley et al., 2016).

Common opal: Opal is a hydrated amorphous form of silica ($\text{SiO}_2 \cdot n\text{H}_2\text{O}$), which contains between 3 and 21 wt. % water (Curtis et al., 2019) and commonly occurs in geothermal areas in association with alunite and jarosite, similar to what is observed in this study. It constitutes a major component of silica sinters, deposited from both near-neutral pH alkali-chloride and acid-sulfate thermal waters, and of silica residues formed at the surface of geothermal fields (Rodgers et al.,

2004). Normally, silica precipitating at the surface do not crystallize in form of crystalline quartz but build amorphous structures such as common opal.

Silica scaling, including common-opal precipitation, represents one of the major technical problems for the geothermal energy production in Indonesia and elsewhere. Massive silica scaling was reported in several operating plants, such as in Dieng, Central Java (Setiawan et al., 2015; Utami et al., 2014; Pambudi et al., 2015), Wayang Windu, West Java and Darajat (Pranato et al., 2017), West Java (Sinaga and Darmanto 2016).

An effort to mitigate the effect of silica scaling was recently introduced by Okazaki et al., (2021). These authors have measured the scale of silica deposition at the Sumukinawa geothermal station, Japan: a scale sensor permitted to approximate the silica-deposition rate up to temperatures of 300°C.

Barite and celestine: The barium sulphate barite, BaSO_4 , and its strontium analogue celestine, SrSO_4 , form a continuous solid-solution series and are important components of sulphate-rich geothermal systems. Celestine is the less-frequent species from the both endmembers and is mined, for instance, in Queensland Australia (Monecke 2002), in Papua New Guinea (Setiawan et al., 2013), India (Bhushan 2015), and Qatar (Dill et al., 2005).

Celestine along with barite belong to the most frequent and most problematic scaling minerals hampering the productivity and economics of geothermal plants. Considering these implications, numerous studies have been conducted to predict the rates of scale formation using different modelling approaches (Banks 2013; Brehme et al., 2018; Tranter et al., 2021).

Additional to being responsible of irreversible energy loss, these sulphates have a large susceptibility to substitute radioactive and poisonous elements (Ra, Pb) by forming solid solutions with isomorphous radium sulphate RaSO_4 and anglesite, PbSO_4 (Fernández-González et al., 2013; Vinogradov et al., 2013; Rosenberg et al., 2014). The formation and textural structure of such solid solutions in geothermal plants were described by Baticci et al. (2010). The disposal and storage of contaminated material cause enormous costs. The assessment of the mineralogy already in the exploration stage, thermodynamic modelling of BaSO_4 – SrSO_4 – RaSO_4 – PbSO_4 precipitation, and the use of inhibitors (cf. Schreiber et al., 2013) are favourable tasks to minimize disposal problems and the expensive operational challenges associate with the re-location of the radioactive waste.

Calcite: The calcium carbonate CaCO_3 is among the most prominent products of scaling especially in geothermal aquifer system, the precipitation of which is triggered by temperature and pressure changes (Baumann et al., 2017). Even though a lot of efforts were undertaken to minimize the formation of calcite scaling in power plants, the production of geothermal energy is still largely affected by this issue (Mundhenk et al., 2013; Boch et al., 2017; Lee, 2013; Ueckert and Baumann 2019).

3. Fieldwork and samples

Two field campaigns have been conducted in order to collect geothermally relevant surface samples that were

subsequently studied for geochemistry and mineralogy. From this collection, a subset of three was selected for this study because of their interesting infrared spectral features and their variability in mineralogical composition (Figures 1–3). The sampling locations are shown in Figure 4.

Sample SAL1 (6°43'27" S, 106°69'62" E, altitude 102 m above sea level (abbreviated a.s.l.), gathered in the Mount Salak area, comes from a natural travertine outcrop located close to geothermal manifestations occurring as hot springs (Figure 1). It was collected in the discharge area of the system characterized by a neutral pH value of around 7 and a high bicarbonate concentration. The outcrop is close to a series of 37°C warm springs.



Figure 1 - Travertine in the Mount Salak area composed of multiply layered calcite (sample SAL1).

Specimen GOU (8°43'56" S, 121°0'37" E, altitude 770 m above sea level (a.s.l.) relates to the Bajawa field on the Flores Island and was collected in a volcanic area near Mount Inerie. It is classified as a deeply altered basalt breccia (Figure 2). Hydrothermal overprinting is manifested as concentric rings, representing the pathways of hot fluids.

Sample MATA2 (8°50'11" S, 121°3'45" E, altitude 1030 m above sea level (a.s.l.) also comes from the Bajawa field and represents a silica sinter (Figure 3). It was collected near the geothermal power plant Mataloko. The mud pools (water temperature 90°C) and steaming ground of the terrain are indicative for hydrothermal activity and hot-fluid circulation.



Figure 2 - Hydrothermally altered, concentrically zoned basalt breccia from the Bajawa area (sample GOU).



Figure 3 - Silica sinter (sample MATA2) deposited adjacent to the Mataloko geothermal plant on Flores Island which is ongoing precipitating and evidences the modern fluid activity in the field.

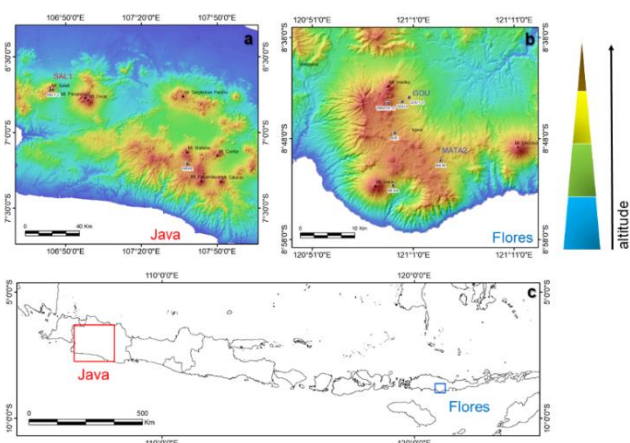


Figure 4 - Maps showing the sample location. (a) Mount Salak (SAL1) on Java (red quadrangle in the lower map); (b) GOU and MATA2 on Flores Island (blue quadrangle in the lower map). These maps are draped on top of the SRTM DEM with hill-shade effect (generated using ArcMap software with illumination azimuth of $N45^{\circ}E$, sun elevation 45° , and z -factor of 0.000009). The color scheme is applied to another SRTM DEM layer (transparency of 40%) to show the elevation differences. (c) Map of Indonesia.

4. Analytical methods

4.1. X-ray powder diffraction

For XRD, the samples were dried at $40^{\circ}C$ for 48 h. Thereafter, these samples were powdered in a Retsch PM200

planetary ball mill for 5 min at 500 rpm for homogenization. Subsequently, the powders were sieved ($212\ \mu m$); the larger particles ($> 212\ \mu m$) were milled again in the Retsch PM200 for 2 min at 650 rpm.

Approximately 0.25 g of the powders were analyzed using a XRD Bruker D2 phaser (Bruker corporation, Billerica, Massachusetts, USA) at the Geoscience Laboratory of the Faculty of Geo-Information Science and Earth Observation, University of Twente, the Netherlands. The equipment operated with $CuK\alpha$ radiation ($1.54\ \text{\AA}$, 10 mA, 30kV) and a LYNXEYE detector. The XRD patterns were collected from 6° to 80° (2θ range) with 0.012° steps and integration time of 0.1s. In addition, a detector slit of 8 mm was used and a standard divergence slit of 0.6 mm was applied to control the illuminated area and enhance the resolution of the measurement. The phase identification was performed using the DIFFRA.EVA software.

4.2. Electron microprobe analysis (EMPA)

Ultra-polished thin sections of the samples were analyzed using a JEOL JXA 8230 electron-probe microanalyzer (JEOL Ltd., Akishima, Japan) at the Microprobe Laboratory of the Section of Inorganic and Isotope Geochemistry at Helmholtz Centre Potsdam GFZ German Research Centre for Geosciences, Germany. Most minerals were measured and identified by EMPA performed in the energy-dispersive mode (EMPA-EDS), using an accelerating voltage of 15kV and a beam current of 20nA. The same analytical conditions were applied in the acquisition of back-scattered electron (BSE) images. Sulphur (S), calcium (Ca), strontium (Sr) and magnesium (Mg) elemental mapping (15 kV, 20 nA) was performed to highlight the spatial and temporal relations of the different species in sample SAL1. The presence of alunite was confirmed by full-quantitative spot analysis conducted in the wavelength-dispersive mode (WDS) at 15 kV, 10 resp. 5 nA, and a slightly defocused beam of $2\ \mu m$.

4.3. SWIR imaging

Hyperspectral images of both intact rock and powdered samples (obtained from the same intact rock) were acquired with a SPECIM SWIR-LVDS-100-N25E camera and OLESMacro lens mounted in a Sisuchema instrument setup (Specim, Spectral Imaging Ltd., Oulu, Finland). The SWIR images captured the wavelength range from 1000 to 2500 nm at $26\ \mu m$ pixel resolution and were 384 pixels wide. They were converted to reflectance images using dark current and white reference measurements. Image noise was reduced by de-striping, bad-pixel removal, and spatial-spectral smoothing (Bakker et al., 2014).

Mineral maps were generated by calculating the wavelength positions of deepest absorption features in wavelength ranges between 1300–1600 nm, 1650–1850 nm, 1850–2100 nm and 2100–2400 nm, following the method of van Ruitenbeek et al., (2014). Decision trees were used to convert the images of the wavelength position data, i.e., wavelength images, into mineral maps (van Ruitenbeek et al., 2017). Mean spectra of the classes in the mineral maps were visually interpreted and classified into (mixtures) of individual minerals.

5. Results

The results of mineral identification are summarized in Table 1 and are reported separately below for each sample and each method.

Table 1 - Mineral phases identified with XRD, EMPA and the SWIR camera SPECIM.

Sample	Location	XRD	EMPA	SWIR camera
SAL1	Salak Mount	calcite	calcite, celestine, gypsum, kaolinite	powder: calcite, gypsum
GOU	Flores	cristobalite, barite, rutile, SiO ₂ polymorph	SiO ₂ polymorph, rutile, barite	rock: alunite, common opal, jarosite
MATA2	Flores	jarosite, alunite, tridymite, barite, ilmenite, SiO ₂ polymorph	alunite, jarosite, barite, ilmenite, SiO ₂ polymorph	rock: alunite, common opal, jarosite. powder ¹ : alunite, common opal, jarosite

¹The powder was obtained from a single rock fragment imaged using SWIR camera then crushed and analyzed by XRD

5.1. SAL1

XRD: The pattern of SAL1 (Figure 5) indicates calcite (major peak at $2\theta = 29^\circ$) as the major phase and additionally implies traces of celestine. Owing to minor abundance, EMPA has been performed to verify the presence of celestine (see the following paragraph).

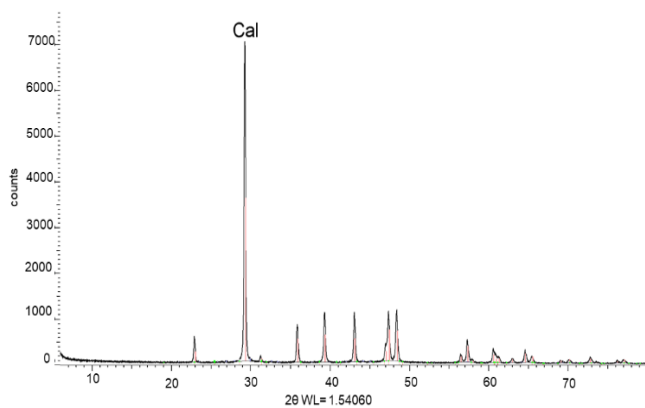


Figure 5 - XRD pattern collected on sample SAL1. Cal = calcite.

EMPA: BSE imaging combined with semi-quantitative EDS analysis reveals the occurrence of calcite and subordinate celestine and, additionally to XRD, a clay mineral (likely kaolinite, $\text{Al}_4[(\text{OH})_8\text{Si}_4\text{O}_{10}]$) and gypsum CaSO_4 (Figures 6a and b).

The elemental distribution maps for S, Ca, Sr, and Mg confirm the occurrence of calcite and celestine and the absence of dolomite $\text{CaMg}(\text{CO}_3)_2$ (Figure 7). In accord with the BSE images, these maps show that early calcite has been replaced by later celestine, gypsum and kaolinite. Moreover, the precipitation of celestine and gypsum is confined to the surface of the rock, implying their formation in response to the infiltration of low-T, sulphate-bearing fluids and with a change in the pH regime, from neutral to acidic.

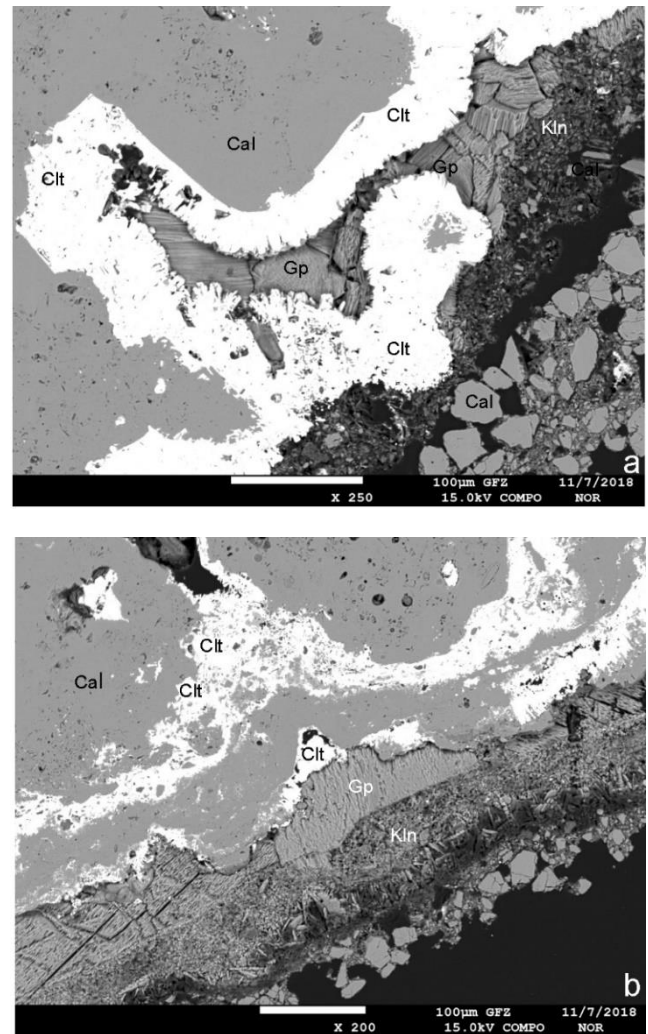


Figure 6 - (a) BSE images of sample SAL1 showing calcite (Cal), celestine (Clt), kaolinite (Kln), and gypsum (Gp). (b) A more detailed image of the sample margin. Mineral abbreviations used here and below are from Whitney and Evans (2010).

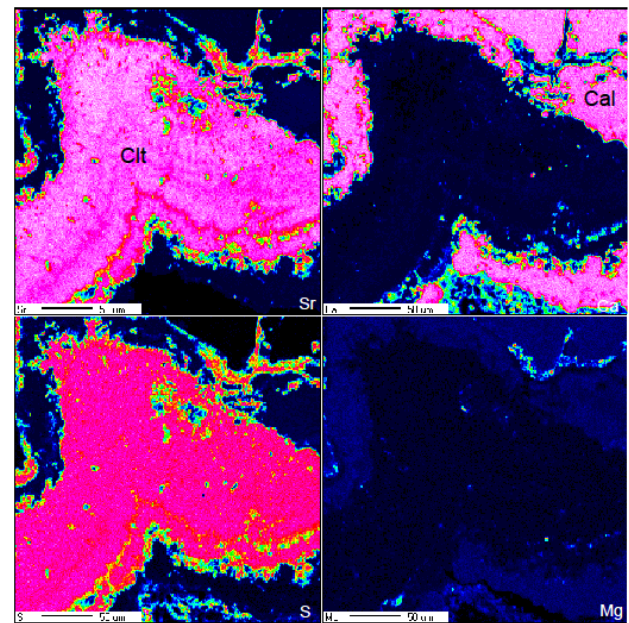


Figure 7- EMPA-generated elemental distribution maps for Sr, Ca, S, and Mg showing a near-surface area of sample SAL1. The coloring is a function of the concentration of the mapped element. The brighter the color, the larger is the concentration of the respective element.

SWIR imaging: The mineral map generated for sample SAL 1 shows that the infrared-detectable mineralogy prominently consists of calcite (Figure 8a). The three end-member spectra (Figure 8b) have a deep, asymmetric absorption feature near 2340 nm typifying calcite. The deep absorption band at 1920 nm is usually related to hydrous phases, such as common opal (Smith et al., 2013; USGS, 2013), gypsum (Harrison, 2017), or a smectite-group mineral (USGS, 2013). The first absorption band at 1450 nm is as well induced by a hydrous phase and, in our case, most likely monitors gypsum (USGS 2013). Small differences between the three recorded spectra reflect minor variations in the inflection points near 2200 and 2195 nm, possibly caused by little variable proportions between calcite and the accompanying minor phases.

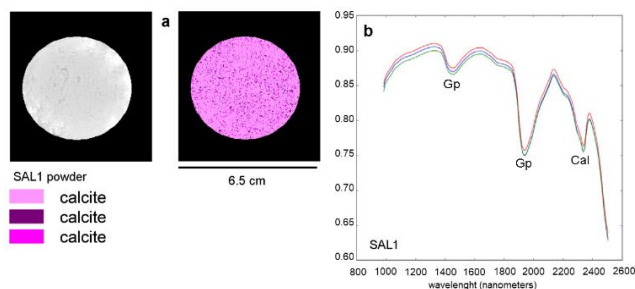


Figure 8 - (a) Mean reflectance (between 1000 and 2500 nm) map (left) and mineral map (right) obtained from hyperspectral imaging of sample SAL1. (b) mean reflectance spectra of the classified pixels of the mineral map in Figure 8a.

5.2. GOU (Flores Island)

XRD: The pattern documents the presence and predominance of cristobalite as well as peaks that could be assigned to minor rutile and barite (Figure 9). The bump in the range of $2\theta = 19$ to 25° is related to amorphous silica, i.e., common opal.

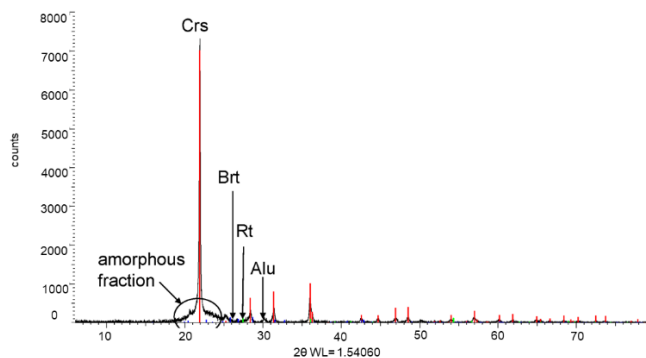


Figure 9 - XRD pattern collected on sample GOU. Crs = cristobalite, Brt = barite, Rt = rutile, Alu = Alunite. The occurrence of minor Brt, Rt and Alu, ideally $KAl_3(SO_4)_2(OH)_6$, were confirmed by EMPA and hyperspectral imaging, respectively. See text for further explanations.

EMPA: BSE imaging (Figure 10) and EDS spot analyses show that the sample is predominantly composed of various SiO_2 polymorphs. Only from the XRD pattern it is evident that both, water-free and water-bearing, crystalline and amorphous varieties of SiO_2 occur. Our interpretation from the texture and appearance of the silica phases is that little altered grains of cristobalite accompanied by weakly to strongly altered, intensely banded, porous, and anhedral grains of common opal coexist in a mostly amorphous finest-grained matrix (Figure 10a). Figure 10b demonstrates that opalized cristobalite is locally accompanied by barite and TiO_2 . The peak position at

$2\theta = 28.5$ in the XRD pattern (cf. Figure 9) indicates that the TiO_2 polymorph is rutile and not brookite or anatase. Alunite was not present in the studied thin section.

SWIR imaging: The mineral map of the intact rock sample implies predominant alunite in variable admixture an amorphous silica phase, such as common opal (Figure 11a). Absorption bands that are typical of alunite are the doublet feature near 1435 and 1490 nm, the sulphate feature near 1760 nm, the deep feature near 2170 nm, and the minor absorption band at 2213 nm (Smith et al., 2013) (Figure 11b). The smaller feature at 2325 nm is attributed to jarosite, ideally $KFe_3^{3+}[(OH)_6(SO_4)_2]$. Common opal is inferred from the pronounced minimum at 1920 nm (Canet et al., 2015). Other minima at 1430 nm and 2200 nm got obscured by the accompanying hydroxylated sulphates. The relative amounts of alunite and common opal vary across the rock as shown in the spatial distribution of the classes in Figure 11b. Note that both the results on the modal mineralogy and the relative proportions of the addressed species (Fig. 11a) are seriously incorrect for the inability to detect crystalline SiO_2 in the SWIR, thus missing abundant XRD-confirmed cristobalite (see section 4.1).

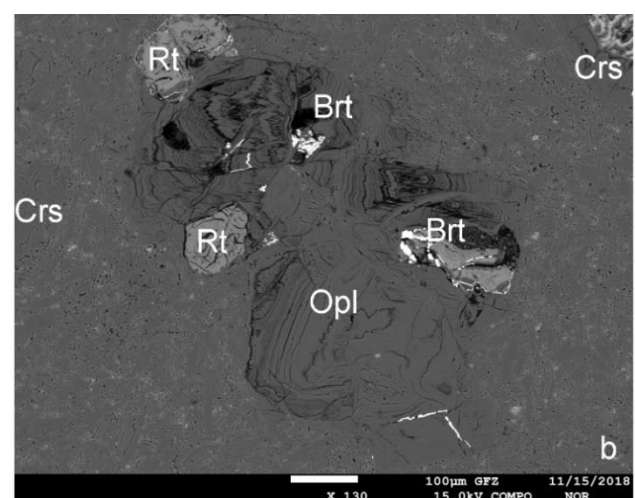
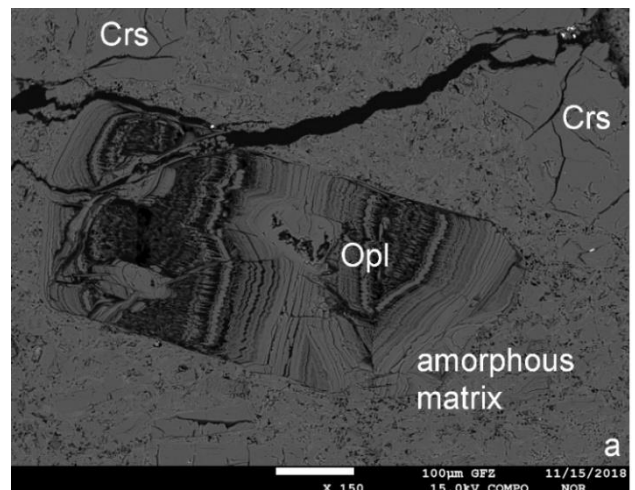


Figure 10 - BSE images of sample GOU. (a) grains of cristobalite (Crs) and altered common opal (Opl) (the darker the in-grain domain the more severe was the overprinting and the more water-rich is the opal) in a dominantly amorphous SiO_2 matrix. (b) common opal grain spatially associated with rutile (Rt) and tiny bright microcrystals identified as barite (Brt). See text for more detailed explanations.

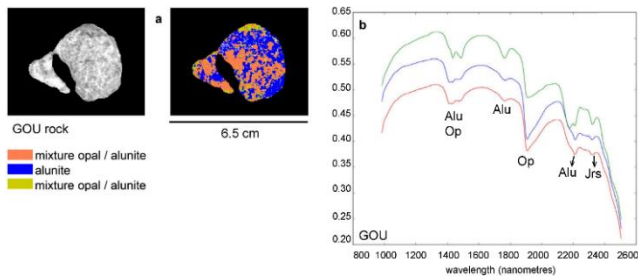


Figure 11 - (a) Mean reflectance (between 1000 and 2500 nm) map (left) and mineral map (right) derived from hyperspectral imaging of sample GOU. (b) Mean reflectance spectrum of the classified pixels of the mineral map.

5.3. MATA2 (Flores Island)

XRD: The pattern is distinguished by a strongly undulating background, which relates to the relatively large fraction of amorphous material in the sample. The bump between 18° and 28° 2θ could be assigned to common opal (Figure 12). Alunite (confirmed by WDS-EPMA), low-T tridymite SiO_2 , and jarosite are identified as major constituents. Minor peaks attest to the presence of subordinate barite and ilmenite FeTiO_3 , the occurrence of which was proven by EDS-EPMA.

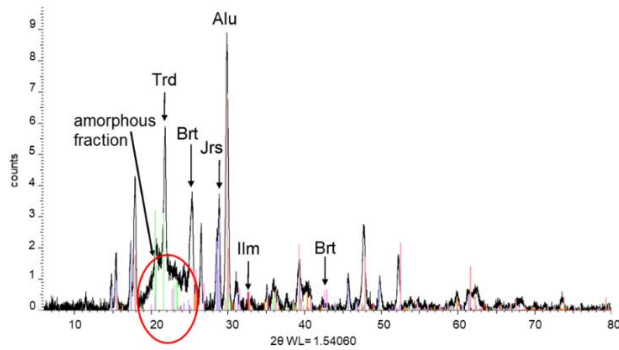


Figure 12 - XRD pattern of the sample MATA2. Alu - alunite, Trd - tridymite, Jrs - jarosite, Ilm - ilmenite, Brt - barite.

EMP: The BSE image (Figure 13) shows several small grains unevenly scattered in a finest-grained matrix. The comparatively bigger grains were identified as a SiO_2 polymorph (low-T tridymite according to XRD) and alunite (see results in table 2). EDS spot analyses reveal that the matrix is dominantly composed of a mixture of alunite, tridymite, jarosite, ilmenite, and barite in varying proportions.

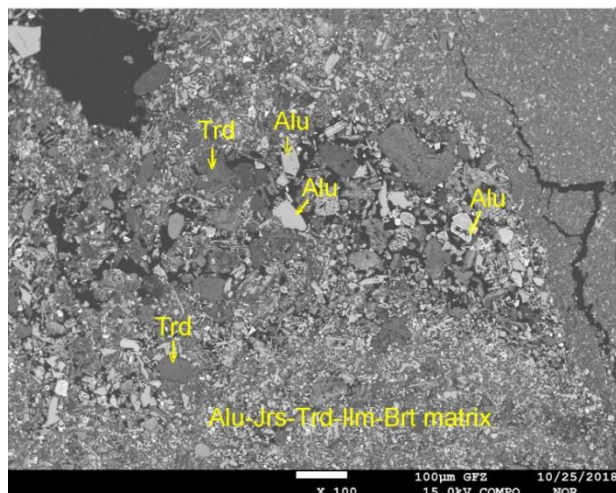


Figure 13 - BSE image of sample MATA2. See Figure 12 for abbreviations.

Table 2 - Representative results of EMP-WDS analyses of alunite from sample MATA2 performed at 15kV, 10 nA, with a slightly defocussed beam of 2 μm .

Label	Al ₂ O ₃ wt. %	K ₂ O wt. %	SO ₄ wt. %	Na ₂ O wt. %	Total ¹ wt. %
MATA 2-1	38.30	2.44	42.43	2.76	85.93
MATA 2-2	37.57	4.60	41.59	2.39	86.15
MATA 2-3	37.01	3.13	41.47	2.42	84.03
MATA 2-5	37.51	6.56	41.27	0.72	86.06
MATA 2-6	39.68	4.05	41.96	3.30	88.99
MATA 2-7	35.74	6.94	40.99	0.97	84.64
MATA 2-8	38.31	3.64	42.02	2.82	86.79
MATA 2-9	38.71	3.92	42.83	2.57	88.03
MATA 2-10	36.88	4.71	40.31	1.29	83.19
MATA 2-13	39.68	4.05	42.33	2.61	88.67
MATA 2-14	35.80	4.27	42.19	1.89	84.15

¹ The low totals relate to the presence of water in alunite.

SWIR imaging: Evaluation of the spectra reveals or infers the occurrence of common opal in association with alunite and minor jarosite. Common opal and alunite can be ascribed to the doublet at 1415 nm, yet a precise differentiation between both is impossible in that particular assemblage. The sharp bands at 1910 and 2213 nm are as well indicative of common opal and alunite (Figure 14). Alunite is also inferred by the small sulphate feature at 1760 nm. The presence of jarosite is implied from the small minimum at 2250 nm.

To examine the degree of spectra agreement for differently prepared rocks, both intact and powdered samples of MATA2 were studied (Figure 14), revealing several mismatches. In the powder spectrum, the jarosite and alunite bands are weaker than those in the rock-fragment spectrum, whereas the common-opal feature appears comparatively stronger. Noteworthy, the quantity ratio between the active minerals is less accurately documented in powdered sample in that the proportion of the dominant species (opal) is overestimated for that of the less abundant minerals (alunite and jarosite).

6. Discussion

The mineral assemblages in the three studied rock samples are largely composed of species, which typically form during natural low- to medium-T geothermal activities and/or precipitate in connection with the operation of geothermal plants (i.e., jarosite, alunite, common opal, tridymite, cristobalite, celestine, barite and calcite). The following discussion of the strengths and weaknesses of the three analytical techniques will focus on these minerals.

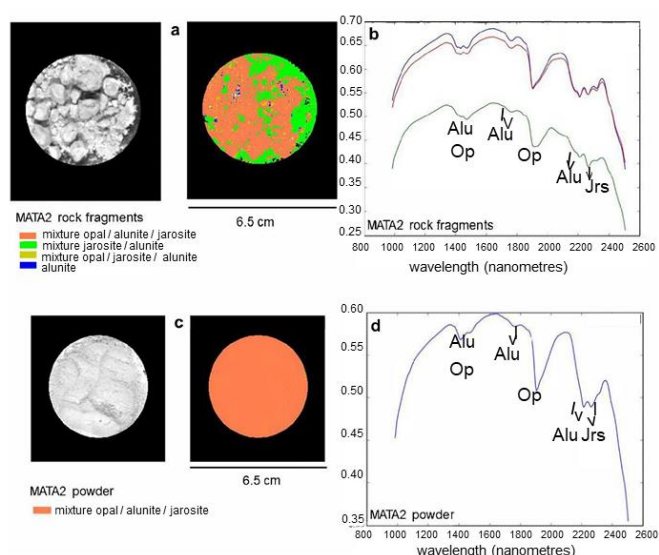


Figure 14 - (a, c) Mean reflectance (between 1000 and 2500 nm) maps (left) and mineral maps (right) received from hyperspectral imaging of fragmented (a) and powdered (c) samples of sample MATA2. (b, d) mean reflectance spectra of the classified pixels of the respective mineral maps.

X-ray diffraction: the use of this laboratory method necessitates a time-consuming sample preparation and evaluation of the raw data, which is even larger if full quantitative information is on the agenda. The strength of XRD is that all crystalline minerals present in our suite of samples at detectable abundance were correctly identified. The detection limit is a function of the minerals present but approximates 2–3 weight percentage. The occurrence of species with similar peak position(s) pose problems owing to peak overlaps. Semi-quantitative mineral compositional data could be acquired under special circumstances, but EMPA is always the better alternative if such information is essential.

Advances relative to EPMA include (a) proof of the occurrence (not nature) of amorphous substances, (ability to discriminate between polymorphs of a substance), and to permit to quantify the modal mineralogy at a reasonable expense.

Electron-microprobe analysis: This method is fast, but relatively expensive and requires a considerable and time-consuming amount of sample preparation and a well-equipped lab. The bulk of crystalline minerals could be unequivocally identified already by EMPA-EDS, which is less labour- and time-intensive as the probe would be operated in WDS mode. EMPA-WDS is mandatory if accurate mineral compositions are required. This technique also permits to study elemental zoning patterns in individual minerals or the detection of phases occurring in considerable minor abundance and in low- μm grain size. Shortcomings include the inability to discriminate between polymorphs of a specific composition, in our case that of SiO_2 (quartz, cristobalite, tridymite) and TiO_2 (rutile, anatase, brookite). Anhydrous silica could be distinguished from (amorphous) hydrous silica (common opal) by EMPA-WDS. Mineralogically heterogeneous rocks require to study more than one single thin section, which only covers an area of roughly 8 cm^2 . Inferences on the quantitative modal composition are

theoretically possible, but extremely time-expensive and thus are not routinely performed.

SWIR imaging: It is a fast and robust method that may take advantage of an outdoors-usable equipment, thus permits on-site measurements. However, any routine use of this technique would be confronted with several serious issues. Many anhydrous sulphates (barite and celestine in our suite of samples) are not detectable in SWIR. Carbonates are SWIR active, but their exact identification is hampered by a lot of interferences. Amorphous minerals (common opal in our samples) are generally not SWIR identifiable due to overlaps with sulphate absorption bands, such as alunite (cf. Figures 11 and 14). The method fails to detect crystalline SiO_2 (in our case tridymite and cristobalite) and feldspars.

Minerals bearing water are spectroscopically active in the short-wave infrared range (SWIR) 1300 to 2500 nm. Water absorbs short wave infrared lights in three wavelengths ranges: 1400, 1900 and 2400 nm (Laukamp et al., 2021). Therefore, hydrated minerals present interesting and diagnostic spectral features in this range if they contain water in their structure in form of OH and H_2O . Hydroxylated sulphate minerals (alunite and jarosite in our sample collection) are thus well suited for SWIR imaging, along with hydrated sulphates as gypsum. Hyperspectral imaging also provides a tool to identify clay minerals, such as kaolinite and smectite. Particularly problematic are inferences on the quantitative modal mineralogy in SWIR-detectable multi-phase samples and practically impossible if SWIR inactive species are present.

In case of compact materials, application is restricted to substances deposited on the rock surface at minimal percentages of roughly 7–10. Problems may also arise if minerals of similar absorption response occur together at similar abundance, thus giving rise to overlapping features and impeding the calculation of reliable quantitative mineral-modal data. Results obtained on intact rock surfaces appear superior for those retrieved from powdered samples. Powders provide a means to detect minerals below the surface, but the relative proportions of the minerals get obscured, i.e., species in large abundance get overestimated for such present in lower percentage.

7. Conclusions

Hyperspectral imaging in the SWIR range, electron-microprobe analysis, and X-ray diffraction analysis are principally suited to study the mineralogy of rocks formed in response to geothermal process in nature and industrial applications. All these methods have their advantages and disadvantages mostly depending on the nature of the precipitated minerals, their absolute and relative modal abundance, their crystallinity, and their grain size. The SWIR camera constitutes a tool that has its strength in the identification of hydroxylated sulphates, carbonates, clay minerals, and amorphous substances absorption-active in the SWIR range. However, its use for the study of geothermally formed mineral assemblages is confronted with several restrictions and limitations (cf. section 5), which does not qualify this tool for a routine and universal use. Although the three analytical techniques applied in this study provide complementary information, EPMA and XRD are superior for SWIR imaging. If high-precision, quantitative and

comprehensive information on rock or scaling mineralogy is required for the sake of safety and productivity of a geothermal plant, their collectively use is warranted.

Acknowledgements

Special thanks go to the Dutch Ministry for Foreign affairs for granting the GEOCAP (Geothermal Capacity Building Programme Netherlands-Indonesia) cooperation and the field campaigns. We would like to thank Freek van der Meer (University of Twente, The Netherlands) for coordinating the GEOCAP cooperation and for his precious inputs during the project and Tia den Hartog (University of Twente) for supporting and organizing the activities in Indonesia. We are thankful to our Indonesian partners Agung Harijoko and Mochamad Nukman (UGM, Yogiakarta, Indonesia) for their help and support in the fieldwork on Flores and many fruitful discussions. The support of Yunus Daud in the planning of the Mount Salak fieldwork is greatly appreciated. Christopher Hecker, Caroline Lievens (University of Twente, the Netherlands) and Muhammad Reza Ramdhan provided valuable support during the Flores field campaign and constructive discussion. We would like to acknowledge the assistance of Franziska Wilke (GFZ Potsdam, Germany) during the electron-microprobe work. The input of David Bruhn (TU Delft, The Netherlands) during the project is appreciated. We would also like to acknowledge Kathrin Zweers-Peters and Ludwig Gröbe (TU Delft, The Netherlands) for XRD-sample preparation and assistance during the measurements. The comments of an anonymous reviewer helped to improve the paper.

References

- Alt-Epping, P., Waber, H.N., Diamond, L.W., Eichinger, L. 2013. Reactive transport modeling of the geothermal system at Bad Blumau, Austria: implications of the combined extraction of heat and CO₂. *Geothermics*, 45, 18–30.
- Arribas, A., Cunningham, C., Rytuba, J., Rye, R., Kelly, W., Podwysocki, M., McKee, E., Tosdal, R. 1995. Geology, geochronology, fluid inclusions, and isotope geochemistry of the Rodalquilar gold alunite deposit, Spain. *Econ. Geol.*, 90, 795–822. <https://doi.org/10.2113/gsecongeo.90.4.795>.
- Bakker, W.H., Van Ruitenbeek, F.J.A., Van der Werff, H.M.A., Zegers, T.E., Oosthoek, J.H.P., Marsh, S.H., Van der Meer, F.D. 2014. Processing OMEGA/Mars Express hyperspectral imagery from radiance-at-sensor to surface reflectance. *Planet. Space Sci.*, 90, 1–9.
- Banks, J. 2013. Sulfate mineral scaling during the production of geothermal energy from sedimentary basin formation brines: A case study at the Groß Schönebeck in-situ geothermal laboratory, Germany. Ph.D. thesis, Freie Universität Berlin, Germany, April 9, 2013.
- Banks, D., Athresh, A., Al-Habaibeh, A., Burnside, N. 2019. Water from abandoned mines as a heat source: practical experiences of open- and closed-loop strategies, United Kingdom. *Sustain. Water Resour. Manag.*, 5, 29–50. <https://doi.org/10.1007/s40899-017-0094-7>.
- Baticci, F., Genter, A., Huttenloch, P., Zorn, R. 2010. Proceedings World Geothermal Congress 2010 Bali, Indonesia, April 25–29, 2010.
- Baumann, T., Bartels, J., Lafogler, M., Wenderoth, F. 2017. Assessment of heat mining and hydrogeochemical reactions with data from a former geothermal injection well in the Malm Aquifer, Bavarian Molasse Basin, Germany. *Geothermics*, 66, 50–60. <https://doi.org/10.1016/j.geothermics.2016.11.008>.
- Bhushan, S.K. 2015. Geology of the Kamthai Rare Earth Deposit. *J. Geol. Soc. India*, 85, 537–546. <https://doi.org/10.1007/s12594-015-0247-y>.
- Boch, R., Leis, A., Haslinger, E., Goldbrunner, E.J., Mittermayr, F., Fröschl, H., Hippler, D., Dietzel, M. 2017. Scale-fragment formation impairing geothermal energy production: interacting H₂S corrosion and CaCO₃ crystal growth. *Geotherm. Energy*, 5. doi: 10.1186/s40517-017-0062-3.
- Bogie, I., Kusumah, Y.I., Wisnandary, M.C. 2008. Overview of the Wayang Windu geothermal field, West Java, Indonesia. *Geothermics*, Volume 37, Issue 3, 347–365. <https://doi.org/10.1016/j.geothermics.2008.03.004>.
- Brehme, M., Deon, F., Haase, C., Wiegand, B., Kamah, Y., Saueter, M., Regenspurg, S. 2016. Fault controlled geochemical properties in Lahendong geothermal reservoir Indonesia. *Grundwasser*, 21, 29–41. <https://doi.org/10.1007/s00767-015-0313-9>.
- Brehme, M., Regenspurg, S., Leary, P., Bulut, F., Milsch, H., Petrauskas, S., Valickas, R., Blöcher, G. 2018. Injection-triggered occlusion of flow pathways in geothermal operations. *Geofluids*, 1–14. <https://doi.org/10.1155/2018/4694829>.
- Canet, C., Hernández-Cruz, B., Jiménez-Franco, A., Pi, T., Peláez, B., Villeanueva-Estrada, R.E., Alfonso, P., González-Partida, E., Salinas, S. 2015. Combining ammonium mapping and short-wave infrared (SWIR) reflectance spectroscopy to constrain a model of hydrothermal alteration for the Acapulco geothermal zone, Eastern Mexico. *Geothermics*, 53, 154–165.
- Curtis, N.J., Gascooke, J.R., Johnston, M.R. 2019. A Review of the classification of opal with reference to recent new localities. *Minerals*, 9, 299. <https://doi.org/10.3390/min9050299>.
- Deon, F., Förster, H., Brehme, M., Wiegand, B., Scheytt, T., Moeck, I., Jaya, M.S., Putriatni D.J. 2015. Geochemical/hydro chemical evaluation of the geothermal potential of the Lamongan volcanic field (Eastern Java, Indonesia). *Geotherm. Energy*, 3, 20. doi:10.1186/s40517-015-0040-6.
- Deyell, C.L., Rye, O.E., Landis, G.P., Bissig, T. 2005. Alunite and the role of magmatic fluids in the Tambo high-sulfidation deposit, El-Indio-Pascua belt, Chile. *Chem. Geol.*, 215, 185–218.
- Dill, H.G., Botz, R., Berner, Z., Stüben, D., Nasir, S., Al-Saad, H. 2005. Sedimentary facies, mineralogy and geochemistry of the sulphate-bearing Miocene Dam Formation in Qatar. *Sediment. Geol.*, 174, 63–96.
- Fernández-González, A., Carneiro, J., Katsikopoulos, D., Prieto, M. 2013. Thermodynamic properties of the (Ba, Pb) SO₄ solid solution under ambient conditions: Implications for the behaviour of Pb and Ra in the environment. *Geochim. Cosmochim. Acta*, 103, 31–43. <https://doi.org/10.1016/j.gca.2012.11.042>.
- Gunnarsson, I., Arnórsson, S. 2005. Impact of silica scaling on the efficiency of heat extraction from high-temperature geothermal fluids. *Geothermics*, 34, 320–9.
- Harrison, T.N. 2017. Experimental VNIR reflectance spectroscopy of gypsum dehydration: Investigating the

- gypsum to basanite transition. *Am. Mineral.*, 97, 598–609.
- Henley, R.W., Ellis, A.J. 1983. Geothermal systems, ancient and modern: A geochemical review. *Earth Sci. Rev.*, 19, 1–50.
- Holley, A.E., Bissig, T., Monecke, T. 2016. The Veladero high-sulfidation epithermal gold deposit, El Indio-Pascua Belt, Argentina: Geochronology of alunite and jarosite. *Econ. Geol.*, 11 (2), 311–330. doi: <https://doi.org/10.2113/econgeo.111.2.311>.
- Jones, B., Jenaut, B.W. 2007. Selective mineralization of microbes in Fe-rich precipitates (jarosite, hydrous ferric oxides) from acid hot springs in the Waiotapu geothermal area, North Island, New Zealand. *Sediment. Geol.*, 194, 1–2, 77–98.
- Johnston, S., Burton, E., Keene, A., Planer-Friedrich, B., Voegelin, A., Blackford, M., Lumpkin, G. 2012. Arsenic mobilization and iron transformations during sulfidization of As (V)-bearing jarosite. *Chem. Geol.*, 334, 9–24. [10.1016/j.chemgeo.2012.09.045](https://doi.org/10.1016/j.chemgeo.2012.09.045).
- Klapper, H.S., Paquette, M., Moeller, M. 2016. Scaling and corrosion behavior of metallic materials after long-term exposure to the geothermal fluid of the North German Basin. *Proceedings of Corrosion Conference and Expo 2016*, Vancouver, Canada, March 6–10, 2016, 3470.
- Koike, K. Kouda, R. 2016. Recent trends of remote sensing technologies applied to metallic mineral and geothermal resources exploration. *J. Min. Mater. Process. Inst. JPN.* 2016, 132, 6, 96–113 (in Japanese with English abstract). <https://doi.org/10.2473/journalofmmij.132.96>.
- Laukamp, C., Rodger, A., LeGras, M., Lampinen, H., Lau, I.C., Pejčić, B., Stromberg, J., Francis, N., Ramanaidou, E. 2021. Mineral Physio-chemistry Underlying Feature-Based Extraction of Mineral Abundance and Composition from Shortwave, Mid and Thermal Infrared Reflectance Spectra. *Minerals*, 11, 347. <https://doi.org/10.3390/min11040347>.
- Lee, K.S. 2013. Aquifer thermal energy storage. *Underground thermal energy storage*, Springer: London, United Kingdom, 2013, pp. 59–93.
- McCubbin, F.M., Tosca, N.J., Smirnov, A., Nekvasil, H., Steele, A., Fries, M., Lindsey, D. 2009. Hydrothermal jarosite and hematite in a pyroxene-hosted melt inclusion in Martian meteorite Miller Range (MIL) 03346: Implications for magmatic-hydrothermal fluids on Mars. *Geochim. Cosmochim. Acta*, 73, 16, 4907–4917. <https://doi.org/10.1016/j.gca.2009.05.031>.
- Monecke, T. 2002. Geology, host rock succession, and hydrothermal alteration of the Waterloo volcanic-hosted massive sulphide deposit (Northern Queensland, Australia). PhD thesis, Technische Universität Bergakademie Freiberg, Germany, 2002.
- Mundhenk, N., Huttenloch, P., Sanjuan, B., Kohl, T., Steger, H., Zorn, R. 2013. Corrosion and scaling as interrelated phenomena in an operating geothermal power plant. *Corros. Sci.*, 70, 17–28.
- Okazaki, T., Kuramitz, H., Watanabe, T., Ueda, A. 2021. Scale sensor: Rapid monitoring of scale deposition and inhibition using fiberoptic in a geothermal system and comparison with other monitoring devices. *Geothermics*, 93. <https://doi.org/10.1016/j.geothermics.2021.102069>.
- Pambudi N.A., Itoi, R., Yamashiro, R., Alam B., Tusara, L., Jalilinasrabad, S., Khasani, J. 2015. The behavior of silica in geothermal brine from Dieng geothermal power plant, Indonesia. *Geothermics*, 54, 109–114. <https://doi.org/10.1016/j.geothermics.2014.12.003>.
- Prananto, L.A., Soelaiman, T.M.F., Aziz, M. 2017. Adoption of Kalina cycle as a bottoming cycle in Wayang Windu geothermal power plant. *Energy Procedia*, 142, 1147–1152. <https://doi.org/10.1016/j.egypro.2017.12.370>.
- Regenspurg, S., Feldbusch, E., Byrne, J., Deon, F., Driba, D.L., Henningses, J., Kappler, A., Naumann, R., Reinsch, T., Schubert C. 2015. Mineral precipitation during production of geothermal fluid from a Permian Rotliegend reservoir. *Geothermics*, 54, 122–135.
- Rodgers, K.A., Hamlin, K.A., Browne, P.R.L., Campbell, K.A., Martin, R. 2000. The steam condensate alteration mineralogy of Ruatapu cave, Orakei Korako geothermal field, Taupo Volcanic Zone, New Zealand. *Mineral. Mag.*, 64, 1, 125–142.
- Rodgers, K.A., Browne, P.R.L., Buddle, T.F., Cook, K., Greatrex, R.A., Hampton, W.A., Herdianita, R., Holland, G.R., Lynne, B., Martin, R., Newton, Z., Pastars, D., Sannazarro, K.L., Teece, C.I.A. 2004. Silica phases in sinters and residues from geothermal fields of New Zealand. *Earth Sci. Rev.*, 66, 1–61. <https://doi.org/10.1016/j.earscirev.2003.10.001>.
- Rosenberg, Y.O., Sadeh, Y., Metz, V., Pina, C.M., Ganor, J. 2014. Nucleation and growth kinetics of $Ra_xBa_{1-x}SO_4$ solid solution in NaCl aqueous solutions. *Geochim Cosmochim. Acta*, 125, 290–307. <https://doi.org/10.1016/j.gca.2013.09.041>.
- Savitri, K.P. 2016. Geology and Geothermal Setting of Tompasso Geothermal System, Indonesia, with Comparisons of Andesite Alteration Patterns with Wairakei, New Zealand. Master Thesis, University of Auckland, Auckland New Zealand, 2016.
- Schreiber, J., Seibt, A., Birner, J., Genter, A., Moeckes, W. 2013. Application of a Scaling Inhibitor System at the Geothermal Power Plant in Soultz-sous-Forêts: Laboratory and on-site Studies. *Proc. of the European Geothermal Congress*, Pisa, Italy, 3–7 June 2013, 3470.
- Şener, M.F., Şener, M., Uysal, I.T. 2017. The evolution of the Cappadocia Geothermal Province, Anatolia (Turkey): geochemical and geochronological evidence. *Hydrogeol. J.*, 25, 8, 2323–2345. [10.1007/s10040-017-1613-1](https://doi.org/10.1007/s10040-017-1613-1).
- Setiawan, A., Panthron, H., Alfredo, D., Perdana, I. 2015. Mitigation of Silica Scaling from Dieng's Geothermal Brines using $Ca(OH)_2$. *Proc. Indonesia International Geothermal Convention and Exhibition 2015 Jakarta Convention Center*, Indonesia, August 19–21, 2015.
- Sinaga, R.H.M., Darmanto, P.S. 2016. Energy Optimization Modeling of Geothermal Power Plant (Case Study: Darajat Geothermal Field Unit III). *Earth Environ. Sci.*, 42 012017. doi:10.1088/1755-1315/42/1/012017.
- Smith, M.R., Bandfield, J.L., Cloutis, E.A., Rice, M.S. 2013. Hydrated silica on Mars: Combined analyses with near-infrared and thermal-infrared spectroscopy. *Icarus*, 233, 633–648.
- Steiner, A. 1977. The Wairakei geothermal area. North Island. New Zealand: Its subsurface geology and hydrothermal rock alteration. *New Zealand Geol. Surv. Bull.*, 90, 1–133.
- Stober, I. 2014. Hydro chemical properties of deep carbonate aquifers in the SW German Molasse basin. *Geotherm. Energy*, 2-13. doi:10.1186/s40517-014-0013-1.
- Taguchi, S., Shimada, Y., Arikado, Y., Motomura, Y., Chiba, H. 2006. Acid alteration at the subsurface of Otake

- geothermal field, Kyushu, Japan. Proceedings of the 28th NZ Geothermal Workshop, Auckland, New Zealand, 2006, 5115.
- Tranter, M., De Lucia, M., Kühn, M. 2021. Numerical investigation of barite scaling kinetics in fractures. *Geothermics*, 91, 102027. <https://doi.org/10.1016/j.geothermics.2020.102027>.
- Ueckert, M., Baumann, T. 2019. Hydro chemical aspects of high-temperature aquifer storage in carbonaceous aquifers: evaluation of a field study. *Geotherm. Energy*, 7, 4. <https://doi.org/10.1186/s40517-019-0120-0>
- U.S. Geological Survey 2013, Spectral library.
- Utami, P., Browne P.R.L. 1999. Subsurface hydrothermal alteration in the Kamojang Geothermal Field, West Java, Indonesia. Proceedings Twenty-Fourth Workshop on Geothermal Reservoir Engineering Stanford University, Stanford, California, January 25–27, 1999. SGP-TR-162
- Utami, P. 2000. Characteristics of the Kamojang Geothermal Reservoir (West Java) as revealed by its hydrothermal alteration mineralogy. Proceedings, World Geothermal Congress 2000, Kyushu-Tohoku, Japan, May 28–June 10, 2000, 1921–1926.
- Utami, P. 2011. Hydrothermal Alteration and the Evolution of the Lahendong Geothermal System, North Sulawesi, Indonesia. Ph.D. Thesis, The University of Auckland, Auckland, New Zealand, 2011.
- Utami, W., Herdianita, R., Atmaja, R. 2014. The Effect of Temperature and pH on the Formation of Silica Scaling of Dieng Geothermal Field, Central Java, Indonesia. Proceedings, Thirty-Ninth Workshop on Geothermal Reservoir Engineering Stanford University, Stanford, California, February 24–26, 2014. SGP-TR-202.
- Van Ruitenbeek, F.J.A., Bakker, W.H., Van der Werff, H.M.A., Zegers, T.E., Oosthoek, J.H.P., Omer, Z.A., Marsh, S.H., Van der Meer, F.D. 2014. Mapping the wavelength position of deepest absorption features to explore mineral diversity in hyperspectral images. *Planet. Space Sci.*, 101, 108–117.
- Van Ruitenbeek, F.J.A., Van der Werff, H.M.A., Bakker, W.H., Van der Meer, F.D., Hecker, C.H., Hein, K.A.A. 2017. Rapid classification of infra-red hyperspectral imagery of rocks with decision trees and wavelength images. http://www.itc.nl/library/papers_2017/pres/vanruitenbeek_rap_ppt.pdf (accessed on 20 September 2019).
- Vinogradov, V.L., Brandt, F., Rozov, K., Klinkenberg, M., Refson, K., Winkler, B., Bosbach, D. 2013. Solid-aqueous equilibrium in the BaSO₄–RaSO₄–H₂O system: First-principles calculations and a thermodynamic assessment. *Geochim. Cosmochim. Acta*, 122, 398–417. <https://doi.org/10.1016/j.gca.2013.08.028>.
- Whitney, D.L., Evans, B.W. 2010 Abbreviations of names of rock forming minerals. *Am. Mineral.*, 95, 185–187. <https://doi.org/10.2138/am.2010.3371>.
- Wu, Y., Li, P. 2020. The potential of coupled carbon storage and geothermal extraction in a CO₂-enhanced geothermal system: a review. *Geotherm. Energy*, 8, 19. <https://doi.org/10.1186/s40517-020-00173-w>.
- Zarrouk, S.J., Woodhurst, B.C., Morris, C. 2014. Silica scaling in geothermal heat exchangers and its impact on pressure drop and performance: Wairakei binary plant, New Zealand. *Geothermics*, 51, 445–459.